

Exploring solar and wind energy resources in North Korea with COMS MI geostationary satellite data coupled with numerical weather prediction reanalysis variables

Jong-Min Yeom^a, Ravinesh C. Deo^b, Jan F. Adamowski^c, Taeyeong Chae^a, Dong-Su Kim^d, Kyung-Soo Han^e, Do-Yong Kim^{f,*}

^a Korea Aerospace Research Institute, Satellite Application Division 115 Gwahangno, Yuseong-gu, Daejeon, 34133, South Korea

^b School of Sciences, Centre for Sustainable Agricultural Systems, University of Southern Queensland, QLD, 4300, Australia

^c Department of Bioresource Engineering, Faculty of Agricultural and Environmental Sciences, McGill University, Montreal, Canada

^d Big Data Application Division, Korea Meteorological Administration, Dongjak-gu, Seoul, 07062, South Korea

^e Department of Spatial Information Engineering, Pukyong National University, Busan, 48513, South Korea

^f Department of Environmental Engineering, Mokpo National University, Muan, 58554, South Korea

ARTICLE INFO

Keywords:

Renewable energy
COMS MI satellite
Numerical weather prediction (NWP)
North Korea
Solar energy
Wind energy

ABSTRACT

Despite their potential as a naturally-available clean energy option, the renewable energy resources of the Democratic People's Republic of Korea (i.e., North Korea) have rarely been evaluated. Therefore, to estimate the availability of land surface solar irradiance necessary for solar applications and to model available energy potential, physically-based models drawing on Communication, Ocean and Meteorological Satellite (COMS) data and associated statistics for key atmospheric constituents, were employed. To assess wind energy resources, model output statistics (MOS) were integrated from post-processed Local Data Assimilation and Prediction System (LDAPS) variables, thereby removing any systematic bias arising from long-term regression methods. The root mean square error (RMSE) and mean bias error (MBE) served to compare pyranometer- and satellite-sourced solar radiation, under instantaneous (87.90 W m^{-2} and 16.84 W m^{-2} , respectively) and daily 'all sky conditions' ($624.98 \text{ Wh m}^{-2} \text{ d}^{-1}$ and $13.89 \text{ Wh m}^{-2} \text{ d}^{-1}$, respectively). These low values indicate that satellite-based solar irradiance is sufficiently accurate to be used to model future land surface solar energy in North Korea. In the evaluation of wind energy resources, daily wind speeds obtained from Numerical Weather Prediction (NWP) reanalysis fields showed good accuracy compared to a meteorological tower measurement ($RMSE = 0.37 \text{ m s}^{-1}$ and $MBE = 0.24 \text{ m s}^{-1}$). In the study region, mean wind energy potential (from 2013–2015) was $3.44 \text{ kWh m}^{-2} \text{ d}^{-1}$, whereas solar energy potential was slightly lower at $3.36 \text{ kWh m}^{-2} \text{ d}^{-1}$; this can be attributed to the nation's mountainous terrain and high latitude. Although the region's mountainous terrain may be an obstacle for future development of renewable energy infrastructure, these initial annual mean solar and wind power density results illustrate the significant renewable energy potential of North Korea. This situates the country in a position to promote the United Nations Sustainable Development Goal (SDG #7) of integrating cleaner and more sustainable energy resources through solar and wind power.

1. Background review

Actively promoted by the United Nations Development Program's (UNDP) Sustainable Development Goal (SDG) # 7 for 2018–2021, renewable energy technologies have attracted the attention of researchers worldwide [1,2]. The UN's SDG strategy has empowered

many nations to promote cleaner energy options across urban, rural and isolated or semi-isolated regions [3]. In 2015, renewable energy, drawn from several alternative resources (e.g., sunlight, wind, hydro and biomass), accounted for, approximately, a 60% net addition to the global power generating capacity, a portion far greater than that of fossil fuels [4]. Since then, the renewable energy sector has grown steadily

* Corresponding author.

E-mail addresses: yeomjm@kari.re.kr (J.-M. Yeom), Ravinesh.Deo@usq.edu.au (R.C. Deo), jan.adamowski@mcgill.ca (J.F. Adamowski), tbchae@kari.re.kr (T. Chae), dkkim131@korea.kr (D.-S. Kim), kyung-soo.han@pknu.ac.kr (K.-S. Han), dylim1975@mokpo.ac.kr (D.-Y. Kim).

<https://doi.org/10.1016/j.rser.2019.109570>

Received 31 August 2018; Received in revised form 4 November 2019; Accepted 4 November 2019

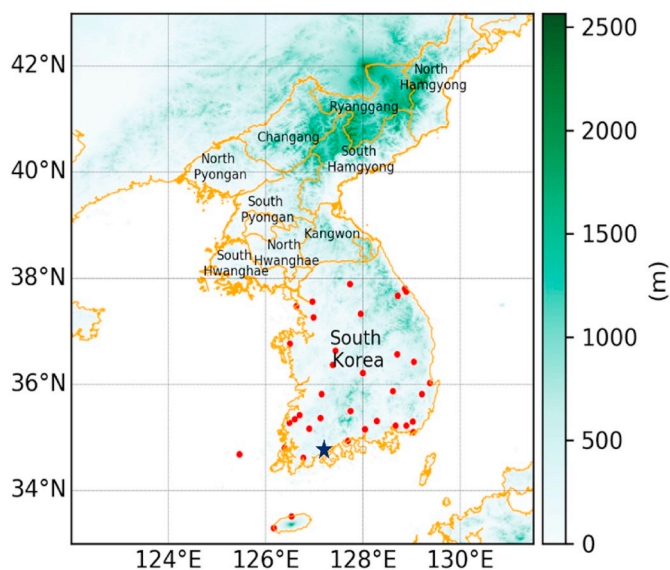
Available online 19 November 2019

1364-0321/© 2019 The Authors.

Published by Elsevier Ltd.

This is an open access article under the CC BY-NC-ND license

(<http://creativecommons.org/licenses/by-nc-nd/4.0/>).



(a)



(b)

Fig. 1. (a) Map of North Korea, the location of meteorological (ground) stations with pyranometers (red dots), meteorological measurement tower (blue star) and digital elevation in the right vertical bar. (b) A photograph of the meteorological measurement tower located in Boseong, South Korea. (For interpretation of the references to color in this figure legend, the reader is referred to the Web version of this article.)

[5]. The increase in global renewable energy demand, especially for solar and wind technologies, can be largely attributed to improvements in renewable energy technologies advocated by SDG 7; compared to conventional fossil fuels, these technologies produce much less CO₂ emissions [1,6–9]. Moreover, these new energy technologies are actively promoted under the UN energy initiatives which strive to make all renewable energy technologies more competitive [10].

The Democratic People's Republic of Korea (*i.e.*, North Korea) is, by many accounts, politically-, socially-, and scientifically-isolated. Consequently, it can be challenging to acquire reliable scientific information (*i.e.*, data gathered through measurements) related to the future potential of renewable energy resources in the region. Moreover, the country itself has not evaluated its renewable energy resources on a national scale. Based on a 2017 CIA report, about 18,400,000 people in North Korea live without electricity, corresponding to an electrification rate of only 30% across the entire population [11]. The lack of electricity contributes significantly to the challenges facing the people of North Korea. The main sources of electrical energy in North Korea are hydroelectric plants and fossil fuels, which account for approximately 55% and 45%, respectively, of the total installed capacity [11]. Notably, the availability of electricity in North Korea often decreases during the winter, when the main river systems that drive hydropower generation freeze, limiting the production of useable power from hydroelectric plants. Official reports on other sources of electrification, especially on the potential of renewable resources, are not readily available [11].

Recent reports describe North Koreans installing low-cost household solar panels to harvest solar energy to address issues of electrical energy insecurity [12]. Unlike hydroelectric and fossil fuel sources, which, under government regulations, are prioritized for large facilities and political areas, solar panels are considered an effective means to resolve the North Korean power shortage. Wind power, another potential resource, is also proving to be a commercially viable energy technology with a very low CO₂ footprint [13]. However, given the technological difficulties associated with wind farm facilities, the harvesting of wind energy in North Korea, particularly in remote locations, has yet to be explored.

The support of international organizations along with that of nearby countries (*e.g.*, the Republic of Korea, *a.k.a.* South Korea), will be essential in aiding North Korea's transition to an energy secure future. Infrastructure and technology transfers will be important in this effort. The extent of North Korea's isolation under the current regime makes this challenging; however, North Koreans still require access to international relief to alleviate their electricity shortages. Aid that benefits the regime (*e.g.*, aid targeted at addressing food shortages) is often prioritized as it provides a useful supply for the North Korean military. Renewable energy facilities, on the other hand, especially those used to produce solar and wind power, are unlikely to be prioritized by the North Korean government as they cannot be used for military purposes due to their relatively low maneuverability and power production [14]. According to a survey conducted by panels of experts from various disciplines and affiliations [15], a contribution of renewable energy by South Korea is considered the best sustainable energy solution for North Korea's chronic energy shortage. However, as mentioned, it is currently difficult to acquire official statistics to continuously and quantitatively monitor the entire nation of North Korea with high spatial and temporal resolution.

The present study aims to create an overview of the size and spatiotemporal distribution of potential renewable energy resources, mainly sunlight and wind, over the entirety of North Korea. Data were drawn from satellite imagery and reanalysis of Numerical Weather Prediction (NWP) data, as well as ground measurements taken near the borders of North Korea. Solar energy resources derived from satellite based-remote sensing data, and wind energy capacity calculated through NWP reanalysis, allowed for a scientific and quantitative estimation of North Korea's exploitable renewable resources. Among the various methods [16,17], a satellite-based physical model was adopted

Table 1
Specifications of geostationary Communication, Ocean and Meteorological Satellite (COMS) Meteorological Imager (MI).

Mission characteristics	Information	Spatial Resolution
Design lifetime	7.5 years from the end of in-orbit test	
Orbit type	Geo-synchronous	
Spectral channels	Visible channel (550–800 nm)	1 × 1 km spatial resolution
	Infrared 1 channel (10,300–11,300 nm)	4 × 4 km spatial resolution
	Infrared 1 channel (10,300–11,300 nm)	4 × 4 km spatial resolution
	Water vapor channel (6500–7000 nm)	4 × 4 km spatial resolution
	SW infrared channel (3500–4000 nm)	4 × 4 km spatial resolution

Table 2
Specifications of the Boseong meteorological tower.

Characteristics	Information	
Location	34.764°N, 127.213°E	
Above mean sea level (AMSL)	2.8 m	
Measurements	Basic meteorological variables	Rainfall, Relative humidity, Greenhouse gas, Sonic anemometer, PM10, PM2.5, Air pollutants, Radiation
	Wind speed and direction	Sensors at 11 levels (10, 20, 40, 60, 80, 100, 140, 180, 220, 260, 300 m)

to monitor North Korea’s more inaccessible regions and generate as much relevant — particularly in terms of atmospheric conditions — high spatiotemporal resolution solar radiation information as possible. In North Korea, where ground pyranometer measurement networks are non-existent or access to their data is restricted, indirect evaluation of solar radiation is generally difficult, whether through interpolation methods [18,19], or through optimization of secondary parameters for use in empirical methods or data-driven (black-box) models drawing on ground records [20–23]. Therefore, the Communication, Ocean and Meteorological Satellite (COMS) Meteorological Imager (MI) channel, integrated within a physical model, was selected to both reflect the complex optical effects of ozone, water vapor, aerosols, and clouds on the atmosphere, and validate estimated solar radiation parameters by ground truthing at sites in South Korea (COMS MI observation coverage area). Geostationary satellites are particularly suited to investigate otherwise inaccessible portions of North Korea as they allow for the monitoring of hourly variations in cloud cover, and offer a broader coverage than high resolution commercial or polar orbit satellites.

Unlike global solar radiation, wind speeds are mainly influenced by topography and elevation; accordingly, many studies have used high-resolution NWP modelling rather than satellite-based products to generate wind resource data, especially for terrestrial regions [24–26]. The scale of NWP modelling for wind resource estimation depends on the spatial scale of the area of interest (AOI). In general, a micro-scale classical computational fluid dynamics (CFD) code coupled with an NWP model serves in evaluating wind resources at the plant scale [27], whereas mesoscale NWP models drawing on observed data are widely used to determine the optimal location of wind power resources at the national scale [28–30]. Although NWP models can be adjusted according to the spatial scale or purpose, systematic errors can still arise given the scarcity of actual data on wind turbine blade rotation intervals that ultimately determine the amount of wind power generated [26,31]. To address these issues, the NWP model’s physical analysis technique can be improved, or statistical corrections (e.g., regression correction and ensemble) can be applied in post-processing after simulating wind resources with the NWP model [32–34,35]. In the present study, a

statistical correction algorithm was applied for simulating wind power resources at turbine height, based on NWP and satellite data.

Ground measurements, such as pyranometer and anemometer datasets, are accurate references with high temporal resolution for solar and wind energy resources, and are often applied for validation (ground truthing) of satellite-based products or optimization of NWP model algorithms. However, it is difficult to evaluate renewable energy resources for large areas, and such information is potentially useful only as a point representation of observed outputs. While remote sensing and NWP models using spatial data are effective tools for estimating an area’s potential resources, their outputs are spatially-estimated values, not true values. Therefore, potential renewable outputs from satellites and NWP models should be used in tandem with ground measurements to validate the estimates [36]. To verify the applicability of the suggested algorithms to the inaccessible areas of North Korea, the reliability of the estimates was confirmed by making full use of ground measurements at meteorological stations in South Korea immediately adjacent to North Korea.

2. Materials and methods

2.1. Characteristics of the study area

Located in East Asia and bordered to the north by China and Russia and to the south by South Korea, North Korea extends over 120,408 km² (37°N to 43°N lat. and 124°E to 131°E long.) and ranges in elevation from sea level to 2744 m (Fig. 1a). Roughly 80% of North Korea is covered by mountains and uplands, suggesting a high potential for wind power. North Korea experiences the combined influence of dryland and oceanic climates. The dominant climate is humid continental, according to the Köppen climate classification scheme [37]. Winters bring clear weather interspersed with snowstorms as a result of northern and northwestern winds that blow in from Siberia. During the summer, the Korean Peninsula receives 60% of its annual rainfall from southern and southeastern monsoons, termed *Jang-Ma* [38]. Owing to its high latitude, during the winter season the country receives little solar radiation; however, this remains a more valuable energy source than hydropower, as North Korea’s small- and medium-sized hydropower plants cannot operate when rivers are frozen, a relatively common condition given the country’s geography and terrain.

Satellite and ground pyranometer datasets were the primary sources for solar radiation estimation and ground truthing. South Korea’s first geostationary satellite, COMS, provides data of observations over the Korean Peninsula and the larger Asia Pacific region at up to 15-min intervals over 24 h. It is a significant contributor to regional weather forecasts and early warnings of high-impact weather events, such as typhoons and torrential rains [39]. Details regarding its functions and outputs are given in Table 1.

A total of 37 ground station pyranometers (Model CM21, Kipp & Zonen, Delft, Holland) [40], installed across the Korean Peninsula (red dots in Fig. 1a), served as sources of validation data to assess the accuracy of satellite-based insolation readings. The pyranometer dataset available from the Korea Meteorological Administration (KMA) provides hourly measurements.

Analysis of wind energy potential was a primary objective of the present study. Accordingly, Local Data Assimilation and Prediction System (LDAPS) NWP data and measured data were obtained from the Boseong meteorological tower (Fig. 1b) — a 307 m tall three-dimensional weather observation system bearing convective and ultra-sonic anemometers as well as other devices (Table 2) — situated at the Boseong Global Standard Observatory and operated by the National Institute of Meteorological Sciences of the KMA. These data were employed to develop NWP output statistics (Fig. 2b) as well as to validate the NWP. The LDAPS provide output at 3-h intervals [41].

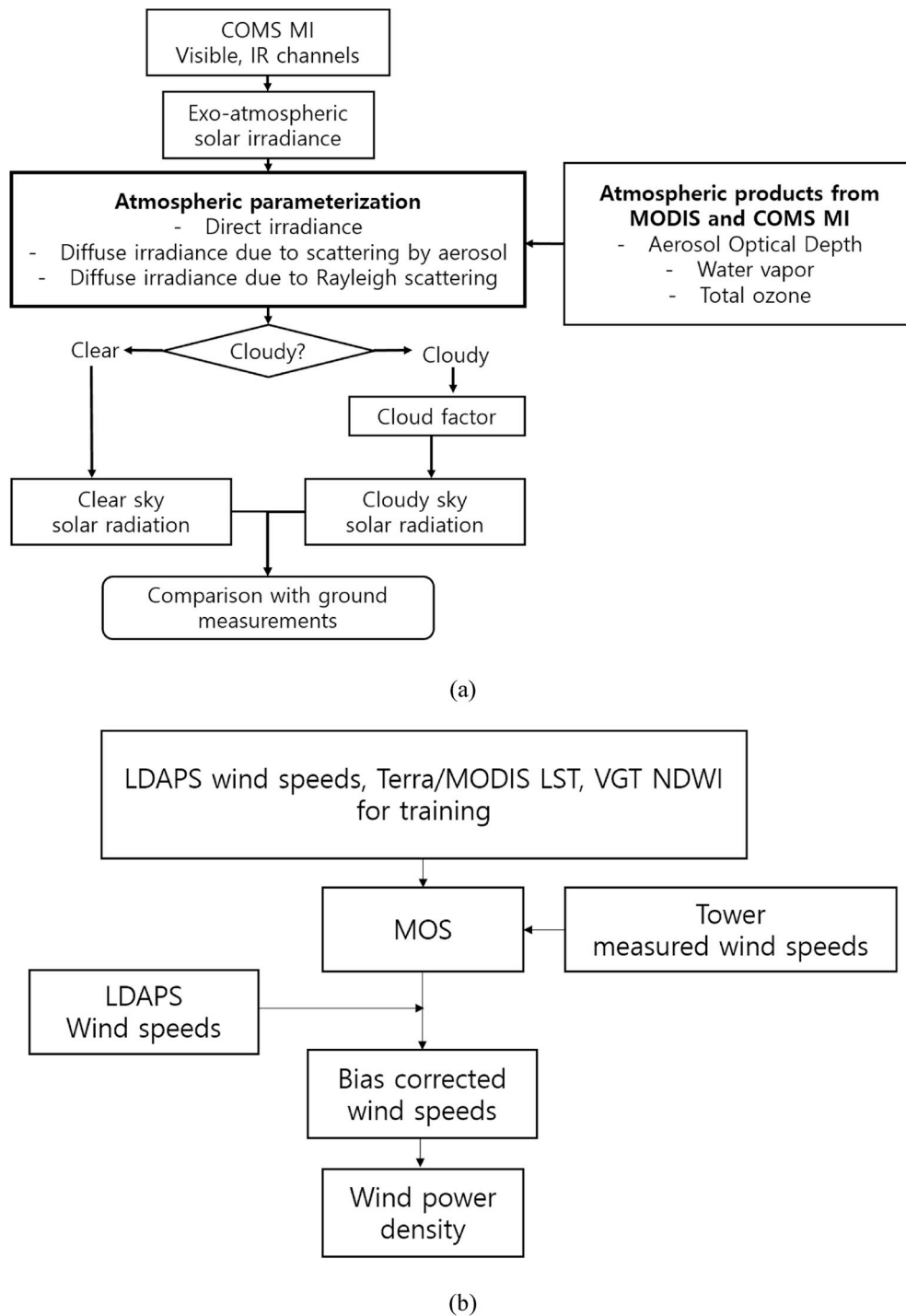


Fig. 2. Flowcharts of the algorithm adopted for estimating solar energy from the COMS MI satellite (a) and wind energy from NWP MOS products (b).

2.2. Physical model algorithms for surface solar insolation using COMS MI satellite data

North Korean solar radiation was estimated using COMS MI geostationary satellite data that reflected the atmospheric conditions of the study area. Pixel-based solar radiation outputs were used given the difficulty in interpreting the effects of atmospheric constituents and clouds on radiation, and the complex physical characteristics and time-consuming calculations necessary to do so [42,43]. Therefore, the current researchers adopted a pixel-based physical model optimized with COMS MI among various satellite-based solar radiation models [44–46].

A flowchart of the solar radiation algorithm integrated with the

COMS MI spectral data (Fig. 2a) shows how: (i) exo-atmospheric (or ‘total’) solar irradiance is calculated based on the Earth-Sun distance and solar zenith angle, and (ii) atmospheric parameterizations considering direct irradiance, diffuse irradiance due to aerosols, and Rayleigh scattering are integrated. Given the reliability of MODIS outputs (e.g., MOD04_L2, MOD05_L2, and MOD07_L2) in parameterizing atmospheric constituents, these were preferentially used; however, when MODIS outputs were unavailable, less spectrally-rich, and therefore less accurate and less desirable COMS MI atmospheric outputs, served as an alternative [47].

Cloud masking was performed to discriminate between clear and cloudy areas. In general, cloud optical and physical properties include a

Table 3
Summary of the specific model configurations.

Parameter	Specification
Horizontal grid	1.5 km (1188 m × 1188 m)
Vertical layers	70 layers (40 km)
Data assimilation	3 dimensional variations
Observations	Surface, Sonde, Aircraft, Scat wind, Radial velocity, Radar-AWS rain rate
Land surface scheme	Joint UK Land Environment Simulator

brighter reflectance and colder temperature than any natural objects on land [48–50]. Accordingly, conventional threshold cloud mask algorithms drew upon COMS MI spectral bands to discriminate cloudy areas through their higher reflectance and colder temperature. The threshold values for the COMS MI visible and IR spectral bands were empirically determined and reflected the Korean Peninsula’s atmospheric characteristics. For pixels deemed ‘cloudy,’ the solar radiation attenuated by the clouds was simulated using a cloud factor, while, for clear areas, the solar radiation from atmospheric parameterization was used. Finally, the estimated surface solar radiation was compared with ground pyranometer observations in South Korea.

Based on the Kawamura physical model [43], COMS MI solar radiation estimates were optimized, especially regarding the cloud factor [42,51], with the cloud-top reflectance and solar zenith angle being considered instead of brightness and temperature since the cloud pass depth is more sensitive to the level of irradiance attenuation [43,51]. Detailed equations for the physical model are as follows [43,51–55]:

$$S = I \left(\frac{d_M}{d} \right)^2 \cos\theta \quad (1)$$

$$S_I = S(\tau_O \tau_R - \alpha_W) \tau_A \quad (2)$$

$$S_R = S \tau_O (0.5(1 - \tau_R)) \tau_A \quad (3)$$

$$S_A = S(\tau_O \tau_R - \alpha_W) F_C \omega_0 (1 - \tau_A) \quad (4)$$

where

- d is the Sun-Earth distance,
- d_M is the mean value of d ,
- F_C is the ratio of forward to total scattering by aerosols,
- I is the solar constant,
- S is the incident solar irradiance,
- S_I is the direct solar irradiance,
- S_R is the diffuse irradiance by Rayleigh scattering,
- S_A is the diffuse irradiance by aerosols,
- α_W is the transmittance of water vapor,
- θ is the incident angle of solar zenith,
- τ_A is the transmittance of aerosols,
- τ_O is the transmittance of ozone,
- τ_R is the transmittance from Rayleigh scattering, and
- ω_0 is the single scattering albedo

Parameters used for the physical model of satellite-based solar radiation are described in detail in previous studies [42,43,51,52,56]. Since the physical models’ solar radiation retrieval process differs according to the existence of clouds, following atmospheric parameterization, cloud masking occurred. Under clear sky conditions, the atmospherically parameterized output of solar radiation was termed clear sky solar radiation (S_{Dclear}):

$$S_{Dclear} = S_I + S_R + S_A \quad (5)$$

Alternatively, should a pixel be determined to be cloudy based on the result of cloud detection, the cloud attenuation effect was considered in

calculating the solar radiation under cloudy conditions (S_{Dcloud}):

$$S_{Dcloud} = (S_I + S_R + S_A) \times Cloud\ Factor \quad (6)$$

where the *Cloud Factor* is the ratio of attenuation by clouds for incident solar radiation using the COMS MI visible band and the solar zenith angle [51]. Using the COMS MI visible channel, cloud top reflectance was observed to indirectly determine cloud optical thickness, *i.e.*, the amount of radiation that penetrates the cloud decreases as cloud reflectance increases. Additionally, given that cloud attenuation of incident solar radiation depends on the cloud pass depth [52], the solar zenith angle over the cloudy area was used in determining cloud effects.

In the case of input parameters such as aerosol optical depth (AOD), water vapor, and total ozone, reliable satellite products from MODIS were mainly used. The COMS MI, a geostationary satellite, provided hourly atmospheric measurements sufficient to parameterize atmospheric effects. The Terra and Aqua satellites only provide twice-a-day data, and their MODIS atmospheric outputs do not meet the temporal resolution requirements for geostationary satellites; however, in the present study, each atmospheric constituent’s daily variation was deemed to be negligible. In the case of AOD, which has the widest variation and contributes significantly to atmospheric effects, the overall root-mean-square error (RMSE, Eq. 11) during the daytime was 0.123 [57], suggesting that the expected error in solar radiation when using daily MODIS outputs would be of little significance. In addition, as MODIS and COMS MI atmospheric outputs like aerosols, water vapor, and ozone were not available for cloudy days, climatological records of aerosols and ozone were used.

2.3. Statistical correction algorithms for wind power resources at turbine height using NWP and satellite data

Developed by the United Kingdom Meteorological Office [58], LDAPS was adopted by the KMA as an operational numerical weather prediction system with specific features (Table 3). Wind speed in North Korea was estimated using LDAPS data (1.5 km horizontal resolution, 70 layers covering ≈ 40 km vertical resolution) provided by the KMA. The JULES (Joint UK Land Environment Simulator) land surface scheme, a type of Unified Model (UM), was combined with Korean observation systems to balance ground physics and optimize real-time weather conditions using a 3-dimensional variation method.

While LDAPS can successfully simulate 3-dimensional wind fields, thereby enabling the estimation of winds at any given elevation, it still suffers from data biases. Remotely-sensed measurements of wind velocity at the ground surface were used to capture systematic bias in wind speed at turbine height. This bias was corrected using a statistical method [32] which used Land Surface Temperature (LST) and normalized difference water index (NDWI) satellite data (Fig. 2b), obtained from Terra/MODIS and SPOT/VEGETATION (VGT) measurements, respectively. A simple algorithm-based multi regression polynomial analysis method, ‘model output statistics’ (MOS), was performed on 75% of the daily wind speed data acquired at wind turbine height (80 m above ground level in South Korea). The remaining 25% of daily wind speeds were randomly used for model evaluation.

$$SPD = f(SPD, LST, NDWI) = A_0 + B_1 \cdot SPD + B_2 \cdot LST + B_3 \cdot NDWI \quad (7)$$

$$(A_0, B_1, B_2, B_3) = (2.3537, 0.8890, -0.0401, 2.2227) \quad (8)$$

where SPD is the wind speed.

To compare solar and wind energy potentials in the same units, the wind energy density ($W\ m^{-2}$) was calculated using air density (ρ) and wind speed:

$$Wind\ power\ density = \rho \cdot SPD^3 \quad (9)$$

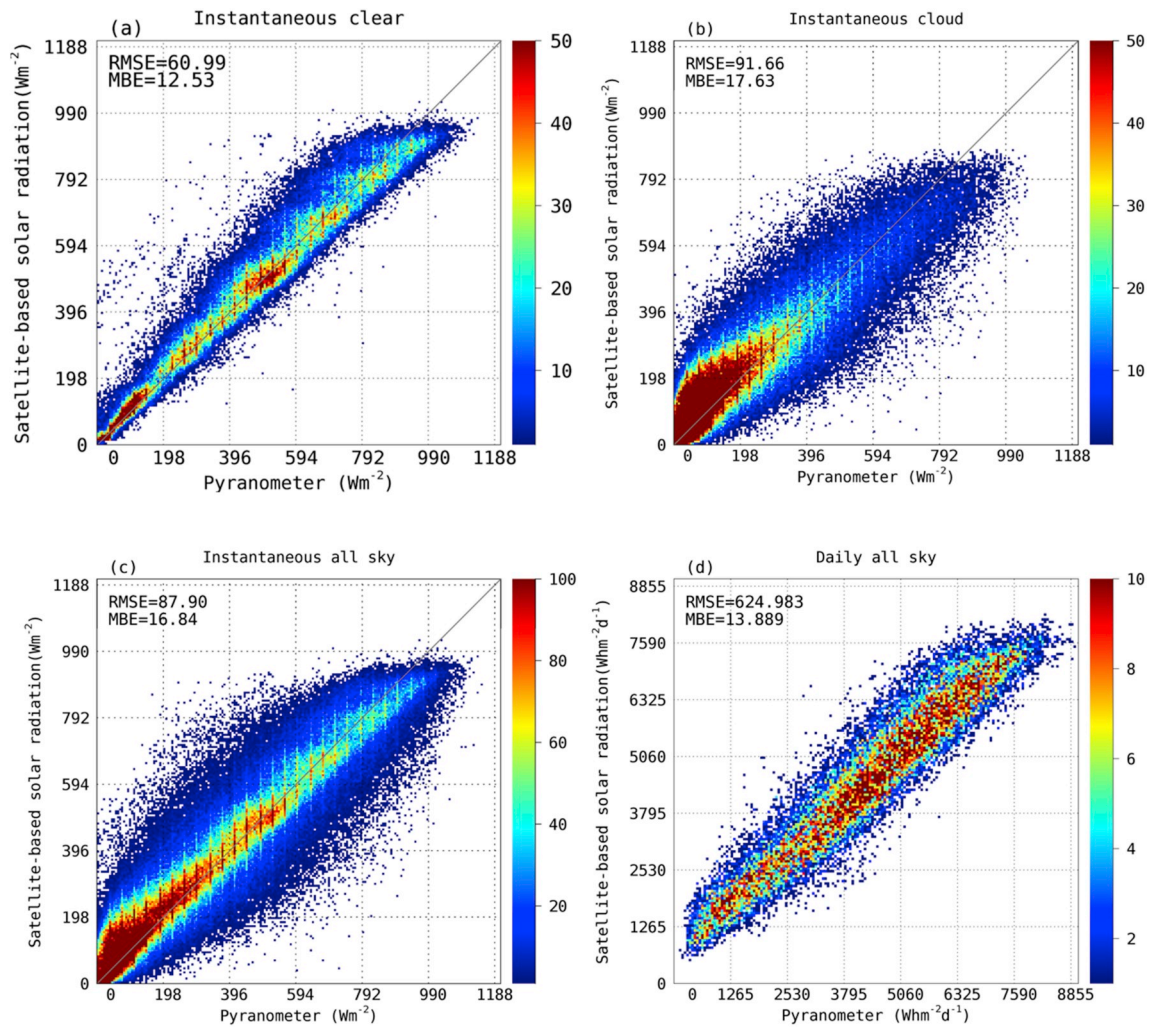


Fig. 3. Density scatter plots for COMS MI satellite-based solar radiation vs. ground pyranometer measurements obtained from the Korean Meteorological Agency (KMA). Panels (a), (b) and (c) represent the instantaneous clear, instantaneous cloudy, and instantaneous all sky conditions, respectively, whereas panel (d) displays a comparison of the daily instantaneous solar radiation. The vertical color bars on the right indicate the frequency of samples within the binning area. For each panel, the root mean square error (RMSE) and mean bias error (MBE) are included. (For interpretation of the references to color in this figure legend, the reader is referred to the Web version of this article.)

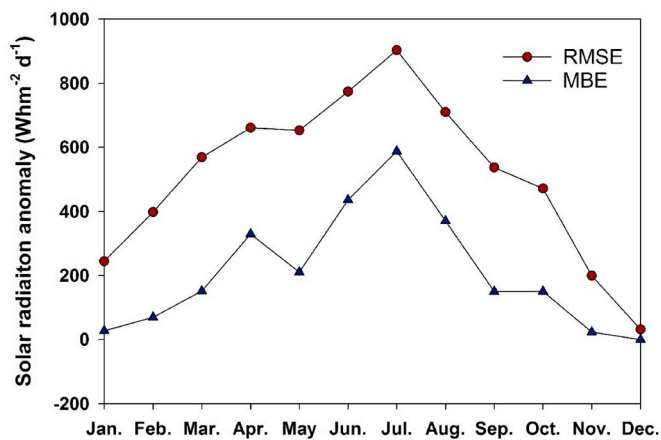


Fig. 4. Seasonal variation in difference between satellite and ground pyranometer measurements of solar radiation for the year 2014. (Includes the root mean square and mean bias errors).

2.4. Evaluation of the magnitude of model error

The magnitude of the modelling error compared to ground measurements was evaluated using two statistical metrics, the mean bias error (MBE) and root mean square error (RMSE):

$$MBE = \frac{1}{n} \sum_{i=1}^{i=n} (y_i^{pred} - y_i^{meas}) \quad (10)$$

$$RMSE = \sqrt{\frac{\sum_{i=1}^{i=n} (y_i^{pred} - y_i^{meas})^2}{n}} \quad (11)$$

where

n is the number of either predicted or measured values,
 y_i^{meas} is the i th measured value,
 y_i^{pred} is the i th predicted value

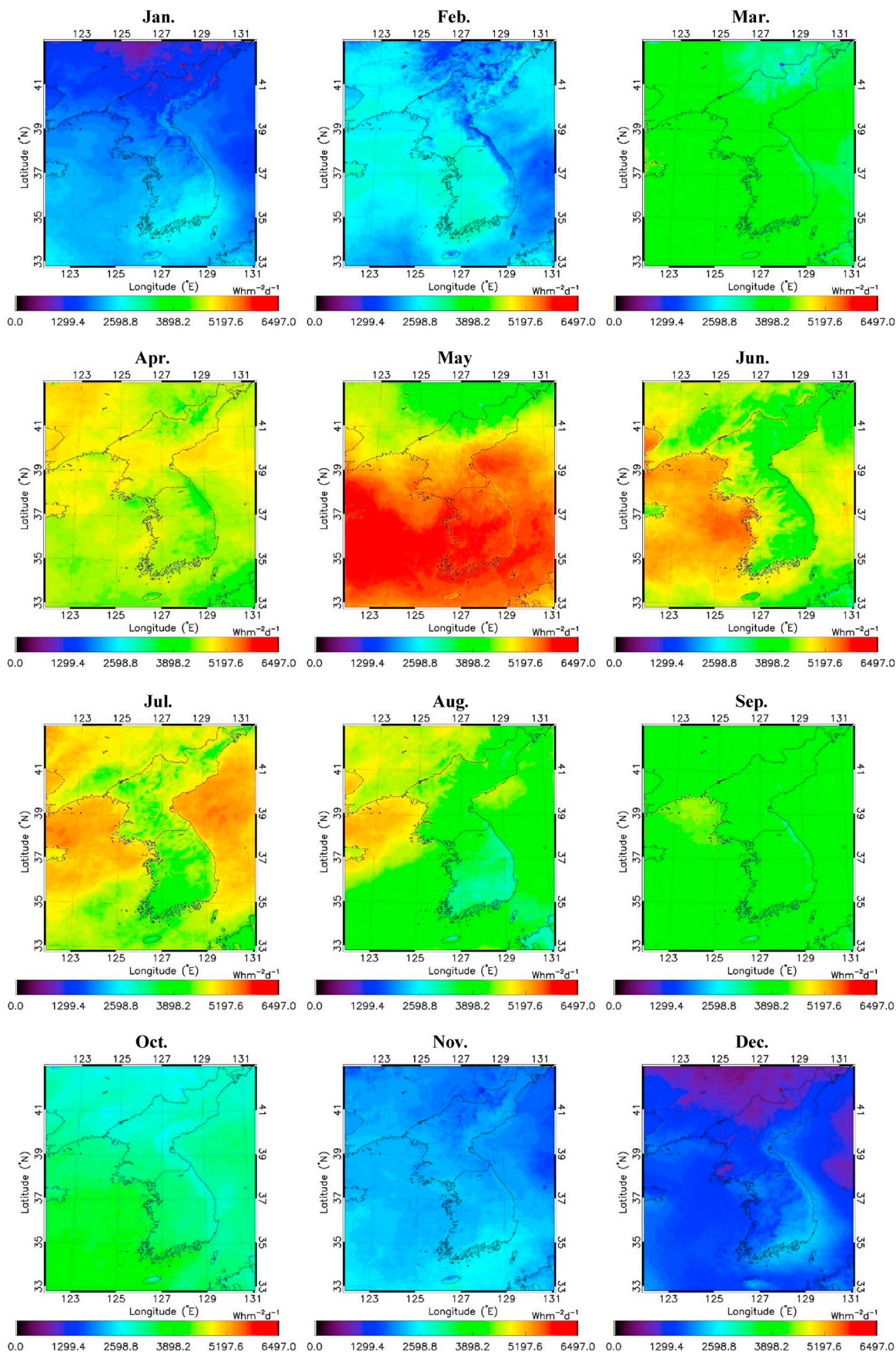


Fig. 5. Spatial maps of monthly solar radiance derived from the COMS MI satellite-based physical model [43] for the Korean Peninsula in 2014.

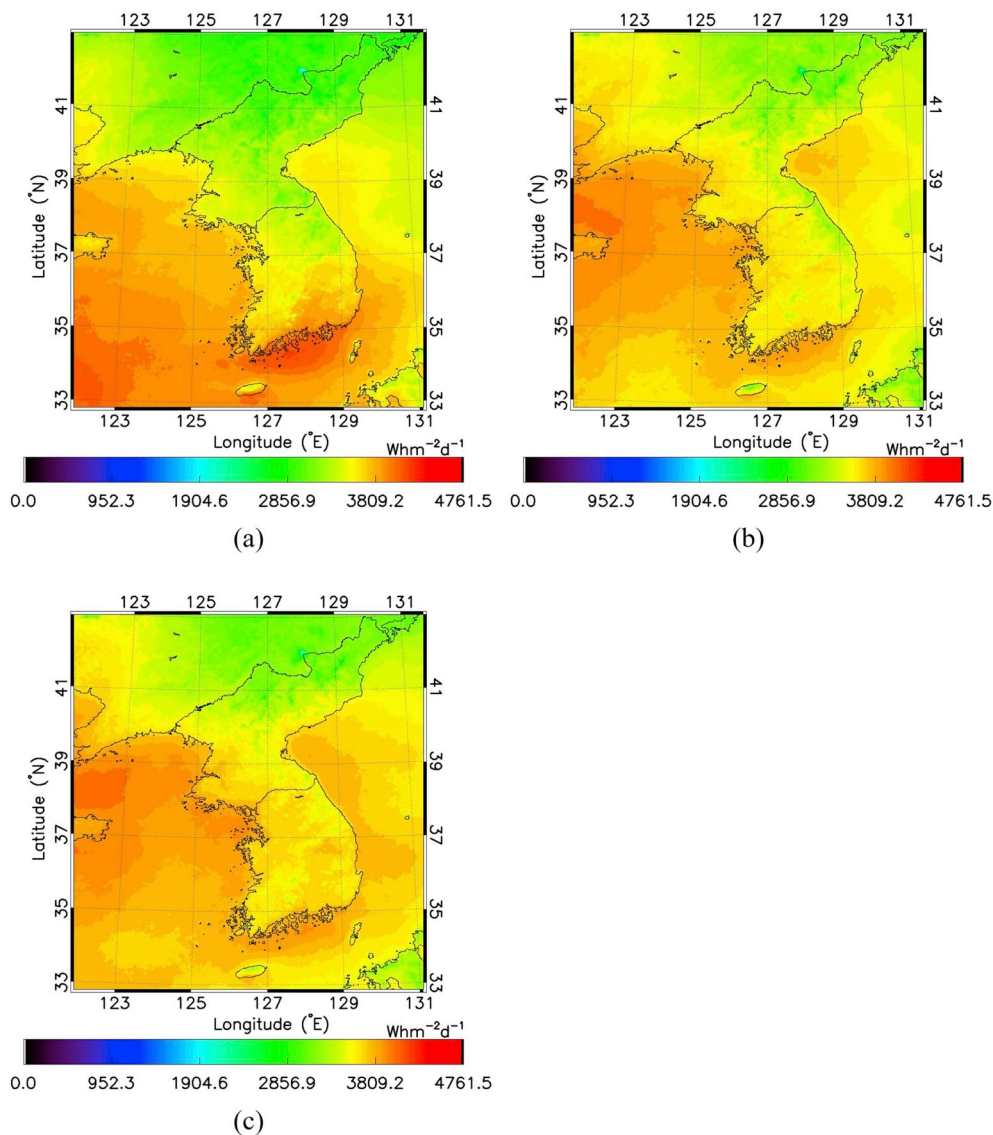


Fig. 6. Maps of the yearly solar radiance over the Korean Peninsula from the COMS MI satellite-based physical model. (a), (b) and (c) are for 2013, 2014, and 2015, respectively.

3. Results

3.1. Mapping solar energy resources using satellite products for the Korean Peninsula

Since the evaluation of the magnitude of potential renewable energy resources is directly related to the accuracy of satellite-based solar radiation outputs, prior to mapping North Korea’s solar energy resource potential, the outputs of the COMS MI satellite were validated against accurate readings from well-calibrated ground pyranometers installed at a number of South Korean meteorological stations [59] (Fig. 1a). Ground pyranometer data served strictly as reference data. Density scatter plots of COMS MI satellite-based solar radiation vs. ground pyranometer measurements of solar radiation, were generated on either:

- instantaneous (hourly, under clear, cloudy, or all sky conditions, Fig. 3a,b,c, respectively), or
- daily cumulated (Fig. 3d),

time scales.

Spatial variation in cloud cover, though complex and challenging to

evaluate, is one of the most important parameters in estimating incident solar radiation. Satellite readings showed a closer clustering to the 1:1 line for instantaneous clear conditions than for instantaneous cloudy conditions. This likely occurred due to the physical model overestimating solar radiation, given that: (i) the fraction of incident solar radiation attenuation by clouds is much greater than that effected by other atmospheric constituents (e.g., aerosols, water vapor or ozone), and (ii) the evaluation of the complex process of cloud attenuation is challenging, leading to the algorithm’s misclassification of thinly-clouded areas as clear areas. Indeed, error statistics for the instantaneous clear sky conditions ($RMSE = 60.99 \text{ W m}^{-2}$, $MBE = 12.53 \text{ W m}^{-2}$) showed greater model accuracy than for cloudy conditions ($RMSE = 91.66 \text{ W m}^{-2}$, $MBE = 17.63 \text{ W m}^{-2}$), or than the accuracy under both conditions combined ($RMSE = 87.91 \text{ W m}^{-2}$, $MBE = 16.84 \text{ W m}^{-2}$). These results indicate that the satellite-based products showed, generally, reliable accuracy, but that a trend of overestimation exists and must be considered.

In the density scatterplot of instantaneous all sky conditions vs. pyrometer-measured ground solar radiation (Fig. 3c), most points lay on or near the 1:1 reference line. Overall, the frequency of the instantaneous all sky condition readings appears to be primarily affected by low

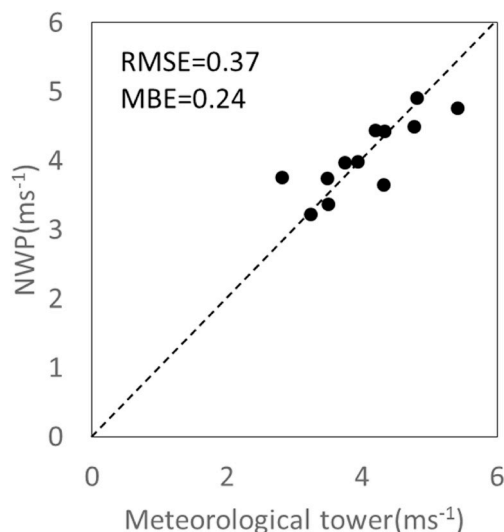


Fig. 7. Scatterplot monthly averaged wind speeds acquired from the Numerical Weather Prediction (NWP) model vs. measured data from the Boseong meteorological tower for the year 2014. The dash line represents the 1:1 reference line. The root mean square and mean bias error are included.

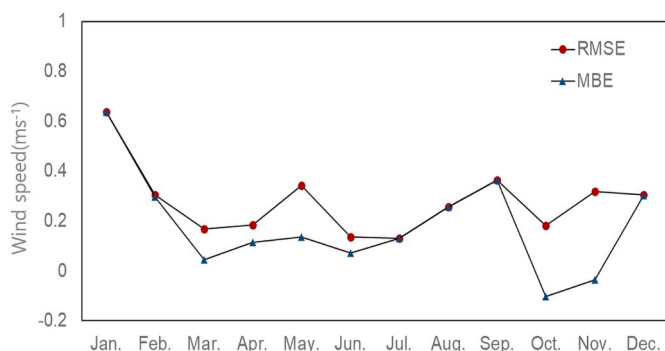


Fig. 8. Seasonal variation in monthly averaged wind speed differences between Numerical Weather Prediction (NWP) estimates and tower measurements for 2014.

solar radiation readings. This is attributable not only to the attenuation of solar radiation by clouds but also to low solar elevation angles at sunrise and sunset, since geostationary satellite observations occur throughout the day.

A comparison of daily cumulated solar radiation from COMS MI and full-day ground measurements showed *RMSE* and *MBE* values of $624.98 \text{ Wh m}^{-2} \text{ d}^{-1}$ and $13.89 \text{ Wh m}^{-2} \text{ d}^{-1}$, respectively — reasonable values, comparable to existing studies [17,35,60,61]. In general, the density scatter plot of the daily all sky conditions solar radiation was seen to converge more densely on the reference 1:1 line than the equivalent scatterplot of instantaneous all sky conditions.

A plot of seasonal variations in differences between satellite- and pyranometer-based solar radiation for 2014 (Fig. 4) shows seasonal uncertainties to be well described, with the lowest deviation occurring in winter ($RMSE = 3.056 \text{ Wh m}^{-2} \text{ d}^{-1}$, $MSE = -0.833 \text{ Wh m}^{-2} \text{ d}^{-1}$), and the greatest in summer ($RMSE = 902.753 \text{ Wh m}^{-2} \text{ d}^{-1}$, $MSE = 586.095 \text{ Wh m}^{-2} \text{ d}^{-1}$) when the mid-latitudes of the Korean Peninsula experience monsoons, which are major contributors to cloudiness. The lower *RMSE* and *MBE* values in the winter can, therefore, be attributed to less cloudiness in the winter [17].

Fig. 5 shows the monthly spatiotemporal variation in the satellite-based solar radiation for 2014, with the summer's high solar resource values indicated in red, and the winter's low solar resource values

indicated in blue. Overall, differences in the quantity of solar radiation with latitude are remarkable, showing that potential solar energy is relatively low in North Korea compared to South Korea. In keeping with high rates of cloudiness being expected in mountainous areas receiving low solar radiation, the fact that variations in solar radiation followed the spatial pattern of mountains was evident in all seasonal cases. Likewise, as a high probability of cloudiness exists in the atmospheric layer over high mountain regions due to physical adiabatic expansion, generally low values of solar radiation were noted in the north-south-extending high mountain ranges of the western portion of the Korean Peninsula. In the case of North Korea, owing to its high latitude and greater expanse of mountains, not only does it receive less solar radiation than South Korea, but its spatial patterns are more complex (Fig. 1a).

The greatest solar radiation in North Korea would be expected to occur between late June and the end of August 2014, when solar elevation is greatest over the mid-latitude region; however, peak solar radiation occurred in May (Fig. 5). This can be attributed to the characteristically high rate of cloud cover expected with the *Jang-Ma*, the East Asian monsoon of mid-latitude regions, which, based on KMA data, began in the southern portion of Korea on June 17, 2014, moved northwards, and ended on July 29, 2014. Indeed, satellite-based observations showed low solar radiation occurred during the summer season (Fig. 5), but these cloudy area observations nonetheless captured spatial variation well [42,51,62]. This observation is particularly relevant to the north-south-extending mountainous area located in the western part of the Korean Peninsula. This area shows spatial oscillation of solar radiation due to the Foehn phenomena caused by strong seasonal winds. In the winter, northwest winds are strong and solar radiation values are low on the mountain range's western slopes, whereas, when the strong southeast winds of the summer (especially in June) prevail, eastern upslope sites experience lower radiation due to a Foehn wall.

Annual spatiotemporal variations in solar radiation over the Korean Peninsula between 2013 and 2015, pictured in Fig. 6, show the inter-annual variability in solar energy resources for the Korean Peninsula to be much lower than its spatial variability, especially where there is complex terrain or a significant latitudinal spread in land mass. Furthermore, the effect of topography on incident solar radiation is more dominant than the effects of weather variability (e.g., East Asian monsoon vs. Foehn wind), as the topographic effect persists over time. Despite the meaningful spatiotemporal analysis results for the Korean Peninsula found in the present study, further exploration of the accuracy of the satellite methodology is suggested to enhance decision-making regarding the stronger solar resource trends.

3.2. Wind power using NWP model methods for estimating wind energy resources

In the case of wind energy resources, the accuracy of the statistically corrected NWP model outputs over the study area was validated against ground measurements. Since tower wind speed measurements serve as standards in many wind power feasibility studies, convective and ultra-sonic anemometer readings of wind speed at a height of 80 m were obtained from equipment mounted on the Boseong meteorological tower (Table 2). These readings stood as the reference for wind speed in evaluating the accuracy of wind fields calculated by the NWP model. Unfortunately, such standardized measurements were only available for 2014. Scatter plots for monthly averaged wind speeds between corrected numerical simulations and tower measurements (Fig. 7) show simulated wind speed to slightly overestimate reference values ($RMSE = 0.37 \text{ m s}^{-1}$, $MBE = 0.24 \text{ m s}^{-1}$). Nonetheless, these results indicate good model performance and compare favorably with those reported in previous studies [63].

Plots of seasonal differences in wind speed values between NWP and meteorological tower measurements allowed for changes in wind energy

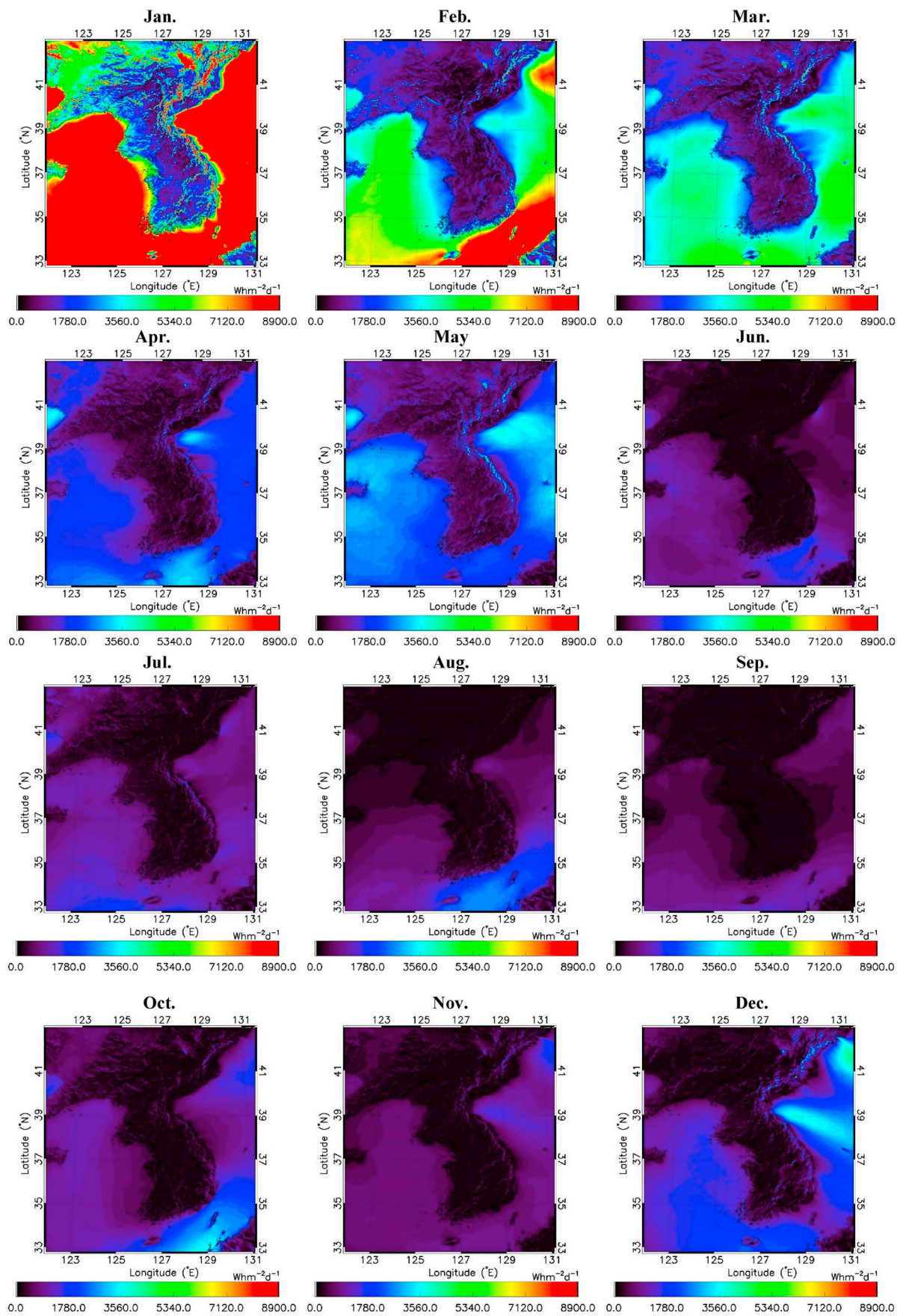


Fig. 9. Maps of monthly potential wind power resources over the Korean Peninsula for 2014, derived from simulated Weather Research and Forecasting (WRF) output.

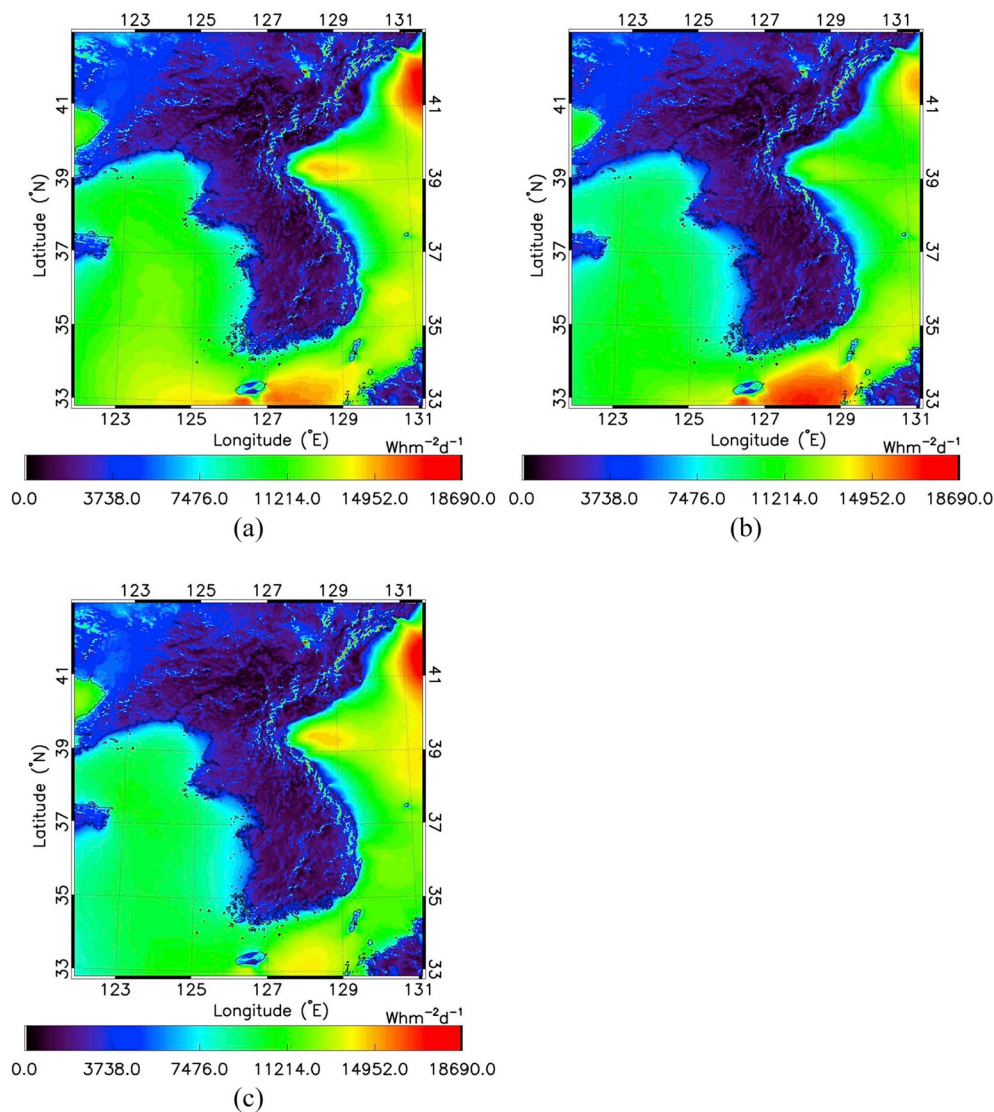


Fig. 10. Maps of annual wind energy resources over the Korean Peninsula based on simulated Weather Research and Forecasting (WRF). (a), (b) and (c) are for 2013, 2014, and 2015, respectively.

potential to be monitored on a seasonal basis (Fig. 8). The associated *RMSE* was high in winter when the Korean Peninsula experiences strong winds, but low in summer, when winds are relatively weak, except during the typhoon season of August to September. Both wind and solar energy resources show characteristic seasonal uncertainty patterns but with opposite trends: for solar radiation, estimation errors increase during the cloudy summer, whereas for wind, uncertainty is associated with the windy winter season.

Monthly temporal variations in NWP-derived wind power density over both land and ocean in 2014 are shown in Fig. 9. The renewable solar energy potential for terrestrial regions is important since current solar panel technology is most often restricted to land; however, in the case of wind energy resources, the renewable energy potential of both land and offshore areas can be exploited [28,64,65]. On land, the sensitivity of wind energy resources to latitude is less than that of solar radiation, with potential energy varying according to the terrain, especially in the high mountain regions. The intensities of energy potential from wind and solar resources exhibit spatially inverse patterns, e.g., high mountains have potentially high wind energy resources due to high wind speeds, but low potential solar energy resources due to the high frequency of cloudiness.

Given the low surface roughness of offshore areas, potential wind

resources are quantitatively and qualitatively greater offshore than on land. However, a seasonal pattern of wind resources exists: the Korean Peninsula, situated between the Asian continent and the North Pacific Ocean, experiences Northwest monsoons in winter due to the Siberian continental air-mass, whilst in the summer a Southeast monsoon generated by the expansion of North Pacific anticyclones prevails. Ocean expanses and coastal areas exhibit more prominent seasonal wind energy trends than land areas. In winter, the potential is generally high due to the strong Northwesterly seasonal winds, which tend to be weak in summer. During the winter season, the spatial characteristics of wind flow show winds escaping from the inland regions towards the east coast of North Korea due to the strong Northwest monsoon.

As with monthly wind energy maps, yearly spatiotemporal variations in wind energy resources over the Korean Peninsula from 2013 to 2015 (Fig. 10) show clear spatiotemporal patterns for both land and sea areas. Offshore regions show relatively greater potential, as higher surface roughness within the atmospheric boundary layer lowers the wind energy potential on land. This pattern is generally consistent with output comparisons between high altitude and offshore wind farms, as described for International Electrotechnical Commission (IEC) class machines operating at 210–320 W m⁻², and generating approximately 5.04–7.68 kWh m⁻² d⁻¹ [66].

Table 4

Evaluation of solar energy potential in the nine administrative provinces and North Korea as a whole for three years (2013, 2014, and 2015).

Region	2013	2014	2015	Overall mean (Standard deviation)
	Mean (Standard deviation)	Mean (Standard deviation)	Mean (Standard deviation)	
	$\text{kWh m}^{-2}\text{d}^{-1}$			
Chagang	3.08 (0.13)	3.35 (0.12)	3.29 (0.12)	3.24 (0.17)
Hamgyong, North	3.04 (0.11)	3.27 (0.12)	3.22 (0.11)	3.18 (0.15)
Hamgyong, South	3.25 (0.12)	3.44 (0.11)	3.50 (0.12)	3.39 (0.16)
Hwanghae, North	3.43 (0.08)	3.63 (0.06)	3.69 (0.07)	3.59 (0.13)
Hwanghae, South	3.53 (0.08)	3.68 (0.06)	3.79 (0.06)	3.67 (0.13)
Kangwon	3.31 (0.09)	3.48 (0.10)	3.59 (0.07)	3.46 (0.15)
Pyongan, North	3.32 (0.07)	3.60 (0.07)	3.54 (0.08)	3.48 (0.14)
Pyongan, South	3.35 (0.12)	3.60 (0.12)	3.62 (0.12)	3.53 (0.17)
Ryganggang	3.01 (0.13)	3.24 (0.13)	3.22 (0.13)	3.16 (0.16)
North Korea	3.24 (0.24)	3.45 (0.20)	3.42 (0.22)	3.36 (0.26)
South Korea	3.64 (0.18)	3.61 (0.11)	3.69 (0.08)	3.65 (0.13)

Table 5

Evaluation of wind energy potential in nine administrative provinces and North Korea as a whole for 2013, 2014 and 2015.

Region	2013	2014	2015	Overall Mean (Standard deviation)
	Mean (Standard deviation)	Mean (Standard deviation)	Mean (Standard deviation)	
	$\text{kWh m}^{-2}\text{d}^{-1}$			
Chagang	1.58 (1.24)	1.50 (1.09)	1.55 (1.09)	1.55 (1.14)
Hamgyong, North	4.09 (3.54)	4.05 (3.40)	4.09 (3.39)	4.08 (3.44)
Hamgyong, South	2.82 (2.53)	2.82 (2.47)	2.96 (2.42)	2.87 (2.48)
Hwanghae, North	2.31 (0.92)	2.18 (0.88)	2.50 (0.98)	2.33 (0.94)
Hwanghae, South	3.78 (1.73)	3.34 (1.47)	3.56 (1.48)	3.56 (1.57)
Kangwon	3.16 (2.66)	3.19 (2.49)	3.35 (2.44)	3.23 (2.53)
Pyongan, North	2.38 (1.20)	2.22 (1.05)	2.23 (1.09)	2.28 (1.12)
Pyongan, South	2.40 (1.32)	2.39 (1.23)	2.67 (1.30)	2.49 (1.29)
Ryganggang	2.88 (2.61)	2.83 (2.48)	2.82 (2.27)	2.84 (2.46)
North Korea	3.54 (2.21)	3.31 (2.04)	3.47 (2.06)	3.44 (2.11)
South Korea	2.97 (2.16)	2.76 (1.93)	2.90 (1.92)	2.88 (2.01)

3.3. Evaluation of solar and wind potential energy resources in North Korea

As mentioned, North Korea exhibited lower solar energy potential than South Korea over the period from 2013 to 2015, largely owing to its higher latitudes and more mountainous regions. In the current study, for the convenience of spatial analysis, the small administrative districts belonging to the larger provinces are included in the provinces. Accordingly, a total of nine large provinces were used as the administrative regions of North Korea (Fig. 1a and Table 4). The mean solar energy potential in North Korea during the three-year period was $3.36 \text{ kWh m}^{-2} \text{ d}^{-1}$ (Table 4), which is lower than South Korea's average of $3.65 \text{ kWh m}^{-2} \text{ d}^{-1}$.

North Korea's solar energy potential is reasonably large, and solar power plants may still be feasible in the region. Moreover, reflecting the geographical characteristics of North Korea, the spatial standard deviation (in parentheses in Table 4) is greater in North Korea than in South Korea, and, therefore, site analysis for photovoltaic (PV) installations will be more important for developing renewable energy resources in North Korea. In comparison with neighboring China's renewable energy potential (2015) of $3.93 \text{ kWh m}^{-2} \text{ d}^{-1}$ [17], North Korea's annual solar energy potential ($3.43 \text{ kWh m}^{-2} \text{ d}^{-1}$) is substantial; North Korea's overall energy potential is comparable to China's solar energy resources, given that China's Qinghai-Tibet Plateau and Taklimakan Desert have relatively low cloudiness.

In 2015, of the nine provinces in North Korea, South Hwanghae exhibited the highest renewable energy resources potential at $3.79 \text{ kWh m}^{-2} \text{ d}^{-1}$. The current study considered only short-term data, but the continuously high amount of solar radiation observed during the research period suggests that the South Hwanghae region could sustainably exploit its solar energy resources. Moreover, a considerable area of North Korea is covered by low elevation plains and hills, regions that could be attractive locations for constructing solar resource

facilities in terms of topography.

Based on annual mean values of solar energy (Table 4), Ryganggang province showed the lowest solar energy potential at $3.16 \text{ kWh m}^{-2} \text{ d}^{-1}$, lower still than that of North Hamgyong province ($3.18 \text{ kWh m}^{-2} \text{ d}^{-1}$), which lies in the high latitude region of North Korea. This is possibly due to the fact that Ryganggang province is more mountainous than North Hamgyong province.

Examination of potential wind energy resources in the nine administrative provinces over three years (2013, 2014, and 2015), as well as for North Korea as a whole (Table 5), showed the three-year mean wind energy resource potential of North Korea to be about $3.44 \text{ kWh m}^{-2} \text{ d}^{-1}$, which, unlike solar energy resources, exceeds that of South Korea ($2.88 \text{ kWh m}^{-2} \text{ d}^{-1}$). However, wind energy has a much higher spatial variance than solar energy (Table 5). Because clouds associated with certain types of terrain or regional weather features are intermittent rather than continuous, the solar energy potential can fall to very low values, though it seldom reaches zero, even in extreme cases. Furthermore, incident solar radiation is partially transmitted through clouds. In contrast, wind energy resources are more dependent on the topography than on the geographical location or cloudiness; the flow of an air mass is most strongly influenced by the effects of the terrain on synoptic and microscale circulations. Given the spatial displacement of wind resources' dependence on topographical characteristics, the spatial deviation was higher in North Korea, with its higher mountains and more complex terrain.

4. Conclusions

This study is significant and unique in that it quantitatively assessed the renewable energy potential of North Korea, a generally inaccessible region, using highly reliable satellite data and an NWP model. It serves as a first step towards a comprehensive assessment and mapping of North Korea's potential renewable solar and wind energy resources. As

expected, North Korea, with its highly mountainous terrain, was found to have greater potential wind energy resources, compared to South Korea. North Korea's solar potential was slightly lower than South Korea's because of its higher latitude and somewhat cloudier conditions during certain times of the year. Nevertheless, solar power facilities may be feasible in North Korea if solar energy initiatives like those of South Korea are implemented. Solar power is one potential solution to the current energy shortage in North Korea; however, owing to large spatial variance in solar energy resources in North Korea, further analysis of its mountainous terrain is necessary. With regards to wind energy resources, its spatial deviation was much greater than that of solar energy resources; therefore, more precise and specific wind resource mapping studies incorporating a Geographic Information Systems platform are required before initiating the construction of large-scale complexes for wind power plants.

This study represents a meaningful step towards solving the chronic energy problems of North Korea. If, as is predicted, the country begins to open to outside investment and support [67], the conversations around energy will likely expand beyond public energy supply to include industrialization. Nevertheless, the first step towards identifying possible fixes to the current electricity shortage in North Korea is to quantify present potential solar and wind energy resources. Similar research in identifying and modelling solar energy potential has recently been undertaken using satellite and atmospheric reanalysis data, including machine learning algorithms applied for energy exploration [68–72]. The current study represents an advancement in exploring energy potentials to resolve the current electricity shortages in North Korea, and is a step to meeting the UN's SDG # 7.

Author contribution statement

Jong-Min Yeom: Conceptualization, Methodology, Validation, Visualization, Writing-Original Draft. **Ravinesh Deo:** Formal analysis, Writing-Review and Editing. **Jan F Adamowski:** Writing-Review and Editing. **Taeyeong Chae:** Formal analysis, Funding acquisition. **Dong-Su Kim:** Resources. **Kyung-Soo Han:** Formal analysis, Funding acquisition. **Do-Yong Kim:** Methodology, Validation, Supervision, Writing-Review and Editing.

Acknowledgments

We are grateful to the editor and anonymous reviewers for their helpful comments and suggestions. This study was supported by the Korea Aerospace Research Institute (FR19920). In addition, this work was funded by the Korea Meteorological Administration Research and Development Program under Grant KMI2018-05210.

References

- REN21 Renewables. Global status report. Paris, France: Renewable energy policy network for the 21st century; 2018. 2018.
- IRENA. Global Energy transformation: a roadmap to 2050. Abu Dhabi: International Renewable Energy Agency; 2019.
- UNDP. UNDP Strategic plan, 2018-2021. Special session (executive board of the united nations development programme, the united nations population fund and the united nations Office for project services). New York: United Nations; 2017.
- REN21 Renewables. Global status report. Paris, France: Renewable energy policy network for the 21st century; 2016. 2016.
- REN21 Renewables. Global status report. Paris, France: Renewable energy policy network for the 21st century; 2019. 2019.
- IRENA 2019. Climate change and renewable energy, National policies and the role of communities, cities and regions (Report to the G20 Climate Sustainability Working Group (CSWG)). Abu Dhabi: International Renewable Energy Agency; 2019.
- Zuluaga CD, Álvarez MA, Giraldo E. Short-term wind speed prediction based on robust Kalman filtering: an experimental comparison. *Appl Energy* 2015;156:321–30.
- Song J, Wang J, Lu H. A novel combined model based on advanced optimization algorithm for short-term wind speed forecasting. *Appl Energy* 2018;215:643–58.
- Demirhan H, Renwick Z. Missing value imputation for short to mid-term horizontal solar irradiance data. *Appl Energy* 2018;225:998–1012.
- IRENA. Renewable power generation costs in 2017. Abu Dhabi: International Renewable Energy Agency; 2018.
- Central Intelligence Agency (CIA). The world factbook. 2017. <https://www.cia.gov/library/publications/the-world-factbook/geos/kn.html>. [Accessed 3 February 2017].
- Reuters In North Korea, solar panel boom gives power to the people. <https://www.reuters.com/article/us-northkorea-solar/in-north-korea-solar-panel-boom-give-s-power-to-the-people-idUSKBN0NC2FG20150422>. [Accessed 22 April 2015].
- Archer CL, Jacobson MZ. Evaluation of global wind power. *J Geophys Res* 2005;110:B22110.
- Sin HY, Heo E, Yi SK, Kim J. South Korea citizen's preferences on renewable energy support and cooperation policy for North Korea. *Renew Sustain Energy Rev* 2010;14:1379–89.
- Yi SK, Sin HY, Heo E. Selecting sustainable renewable energy source for energy assistance to North Korea. *Renew Sustain Energy Rev* 2011;15:554–63.
- Antonanzas-Torres F, Urraca R, Polo J, Perpiñán-Lamigueiro O, Escobar R. Clear sky solar irradiance models: a review of seventy models. *Renew Sustain Energy Rev* 2019;107:374–87.
- Qin W, Wang L, Lin A, Zhang M, Xia X, Hu B, Niu Z. Comparison of deterministic and data-driven models for solar radiation estimation in China. *Renew Sustain Energy Rev* 2018;81:579–94.
- Alsamamra H, Ruiz-Arias JA, Pozo-Vázquez D, Tovar-Pescador J. A comparative study of ordinary and residual kriging techniques for mapping global solar radiation over southern Spain. *Agric Meteorol* 2009;149(8):1343–57.
- Ruiz-Arias JA, Pozo-Vázquez D, Santos-Alamillos FJ, Lara-Fanego V, Tovar-Pescador J. A topographic geostatistical approach for mapping monthly mean values of daily global solar radiation: a case study in southern Spain. *Agric Meteorol* 2011;151(12):1812–22.
- Besharat F, Dehghan AA, Faghhih AR. Empirical models for estimating global solar radiation: a review and case study. *Renew Sustain Energy Rev* 2013;21:798–821.
- Ertekin C, Evrendilek F. Spatio-temporal modeling of global solar radiation dynamics as a function of sunshine duration for Turkey. *Agric For Meteorol* 2007;145(1):36–47.
- Hargreaves GH. Simplified for estimating monthly solar radiation in North America and Europe. Logan, Utah: Utah State University; 1994.
- Allen RG. Self-calibrating method for estimating solar radiation from air temperature. *J Hydrol Eng ASCE* 1997;2(2):56–67.
- Yim SHL, Fung JCH, Lau AKH, Kot SC. Developing a high-resolution wind map for a complex terrain with a coupled MM5/CALMET system. *J Geophys Res* 2007;112:D05106.
- Salcedo-Sanz S, Pérez-Bellido AM, Ortiz-García EG, Portilla-Figuera A, Prieto L, Paredes D. Hybridizing the fifth generation mesoscale model with artificial neural networks for short-term wind speed prediction. *Renew Energy* 2009;34:1451–7.
- Fernández-González S, Martín ML, García-Ortega E, Merino A, Lorenzana J, Sánchez JL, Valero F, Rodrigo JS. Sensitivity analysis of the WRF model: wind-resource assessment for complex terrain. *J Appl Meteorol Climatol* 2018;57:733–53.
- Temel O, Bricteuz L, van Beeck J. Coupled WRF-OpenFORM study of wind flow over complex terrain. *J Wind Eng Ind Aerodyn* 2018;174:152–69.
- Kim DY, Kim JY, Kim JJ. Mesoscale simulations of multi-decadal variability in the wind resource over Korea. *Asia-Pacific J Atmos Sci* 2013;49(2):183–92.
- Kim JY, Kim DY, Oh JH. Projected changes in wind speed over the Republic of Korea under A1B climate change scenario. *Int J Climatol* 2014;34:1346–56.
- Gómez I, Caselles V, Estrela MJ, Sánchez JM, Rubio E. Simulation of surface energy fluxes and meteorological variables using the Regional Atmospheric Modeling System (RAMS): evaluating the impact of land-atmosphere coupling on short-term forecasts. *Agric For Meteorol* 2018;249:319–34.
- Ohunakin OS, Adaramola MS, Oyewola OM. Wind energy evaluation for electricity generation using WECS in seven selected locations in Nigeria. *Appl Energy* 2011;88(9):3197–206.
- Kim DY, Kim JY, Kim JJ. A regression based statistical correction of mesoscale simulations for near-surface wind speed using remotely sensed surface observations. *Asia-Pacific J Atmos Sci* 2012;48(4):449–56.
- Sideratos G, Hatzigiorgiou ND. An advanced statistical method for wind power forecasting. *IEEE Trans Power Syst* 2007;22(1):258–65.
- Bessac J, Constantinescu E, Anitescu M. Stochastic simulation of predictive space-time scenarios of wind speed using observations and physical model outputs. *Ann Appl Stat* 2018;12:432–58.
- Ryu Y, Jiang C, Kobayashi H, Detto M. MODIS-derived global land products of shortwave radiation and diffuse and total photosynthetically active radiation at 5 km resolution from 2000. *Remote Sens Environ* 2018;204:812–25.
- Polo J, Wilbert S, Ruiz-Arias JA, Meyer R, Gueymard C, Sári M, Martí L, Mieslinger T, Blanc P, Grant I, Boland J, Ineichen P, Remund J, Escobar R, Troccoli A, Sengupta M, Nielsen KP, Renne D, Geuder N, Cebecauer T. Preliminary survey on site-adaptation techniques for satellite-derived and reanalysis solar radiation datasets. *Sol Energy* 2016;132:25–37.
- Peel MC, Finlayson BL, McMahon TA. Updated world map of the Köppen-Geiger climate classification. *Hydrol Earth Syst Sci* 2007;11:1633–44.
- KMA. Annual report 2015. Seoul, Korea: Korea Meteorological Administration; 2015. http://www.kma.go.kr/download_01/Annual_Report_2015.pdf. [Accessed 28 October 2019].
- NMSC KMA. COMS meteorological data processing system (CMDPS) algorithm theoretical basis document (ATBD). Seoul, Korea: National Meteorological Satellite Center of Korea Meteorological Agency; 2009. <http://203.247.66.167/html/hompage/en/ver2/static/selectStaticPage.do?view=satellites.coms.operations.selectATBT#none>. [Accessed 28 October 2019].

- [40] Kipp & Zonen. Instruction manual, CM21 precision pyranometer. 2004. <https://www.kippzonen.com/Download/52/CM-21-Pyranometer-Manual>. [Accessed 28 October 2019].
- [41] Park SU, Lee IH, Joo SJ, Ju JW. Emergency preparedness for the accidental release of radionuclides from the Uljin nuclear power plant in Korea. *J Environ Radioact* 2017;180:90–105.
- [42] Yeom JM, Seo YK, Kim D. Solar radiation received by slopes using COMS Imagery, a physically based radiation model, and GLOBE. *J Sens* 2016;2016:1–15.
- [43] Kawamura H, Tanahashi S, Takahashi T. Estimation of insolation over the Pacific Ocean off the Sanriku coast. *J Oceanogr* 1998;54(5):457–64.
- [44] Urraca R, Huld T, Gracia-Amillo A, Martizen-de-Pison FJ, Kaspar F, Sanz-Garcia A. Evaluation of global horizontal irradiance estimates from ERA5 and COSMO-REA6 reanalyses using ground and satellite-based data. *Sol Energy* 2018;164:339–54.
- [45] Otkin JA, Anderson MC. Validation of GOES-based insolation estimates using data from the U.S. climate reference network. *J Hydrometeorol* 2005;6:460–75.
- [46] Urraca R, Martinez-de-Pison E, Sanz-Garcia A, Antonanzas J, Antonanzas-Torres F. Estimation methods for global solar radiation: case study evaluation of five different approaches in central Spain. *Renew Sustain Energy Rev* 2017;77:1098–113.
- [47] Kim J, Yoon JM, Ahn MH, Sohn BJ, Lim HS. Retrieving aerosol optical depth using visible and mid-IR channels from geostationary satellite MTSAT-1R. *Int J Remote Sens* 2008;29(10):6181–92.
- [48] Platnick S, King MD, Ackerman SA, Menzel WP, Baum BA, Riedi JC, Frey RA. The MODIS cloud products: algorithms and examples from Terra. *IEEE Trans Geosci Remote Sens* 2003;41(2):459–72.
- [49] Miller SD, Stephens GL, Drummond CK, Heidinger AK, Partain PT. A multisensory diagnostic satellite cloud property retrieval scheme. *J Geophys Res: Atmos* 2000;105(D15):19955–71.
- [50] Sun L, Mi X, Wei J, Wang J, Tian X, Yu H, Gan P. A cloud detection algorithm-generating method for remote sensing data at visible to short-wave infrared wavelengths. *ISPRS J Photogram* 2017;124:70–88.
- [51] Yeom JM, Han KS, Kim JJ. Evaluation on penetration rate of cloud for incoming solar radiation using geostationary satellite data. *Asia-Pacific J Atmos Sci* 2012;48(2):115–23.
- [52] Kawai Y, Kawamura H. Validation and improvement of satellite-derived surface solar radiation over the northwestern Pacific Ocean. *J Oceanogr* 2005;61(1):79–89.
- [53] Tanahashi S, Kawamura H, Matsuura T, Takahashi T, Yusa H. A system to distribute satellite incident solar radiation in real-time. *Remote Sens Environ* 2001;75(3):412–22.
- [54] Yeom JM, Han KS. Improved estimation of surface solar insolation using a neural network and MTSAT-1R data. *Comput Geosci* 2010;36(5):590–7.
- [55] Yeom JM, Han KS, Kim YS, Jang JD. Neural network determination of cloud attenuation to estimate insolation using MTSAT-1R data. *Int J Remote Sens* 2008;29(21):6193–208.
- [56] Kizu S. A study on thermal response of ocean surface layer to solar radiation using satellite sensing [Ph.D. thesis]. Sendai, Japan: Tohoku University; 1995.
- [57] Green M, Kondragunta S, Ciren P, Xu C. Comparison of GOES and MODIS aerosol optical depth (AOD) to aerosol robotic network (AERONET) AOD and IMPROVE PM2.5 mass at Bondville, Illinois. *J Air Waste Manag Assoc* 2009;59(9):1082–91.
- [58] Walters DN, Best MJ, Bushell AC, Copsey D, Edwards JM, Falloon PD, Harris CM, Lock AP, Manners JC, Morcrette CJ, Roberts MJ, Stratton RA, Webster S, Wilkinson M, Willett MR, Boutle IA, Earshaw PD, Hill PG, MacLachlan C, Martin GM, Moufouma-Okia GM, Palmer MD, Petch JC, Rooney GG, Scaife AA, Williams KD. The met Office unified model global atmosphere 3.0/3.1 and JULES global land 3.0/3.1 configurations. *Geosci Model Dev (GMD)* 2011;4:919–41.
- [59] Paulescu M, Paulescu E, Gravila P, Badescu V. Solar radiation measurements. In: *Weather modeling and forecasting of PV systems operation*. Green energy and technology. London: Springer; 2013. p. 17–42.
- [60] Roupioz L, Jia L, Nerry F, Menenti M. Estimation of daily solar radiation budget at kilometer resolution over the Tibetan Plateau by integrating MODIS data products and a DEM. *Remote Sens* 2016;8:504.
- [61] Tang W, Qin J, Yang K, Liu S, Lu N, Niu X. Retrieving high-resolution surface solar radiation with cloud parameters derived by combining MODIS and MTSAT data. *Atmos Chem Phys* 2016;16:2543–57.
- [62] Watanabe T, Oishi Y, Nakajima TY. Characterization of surface solar irradiance variability using cloud properties based on satellite observation. *Sol Energy* 2016;140(15):83–92.
- [63] Pan L, Liu Y, Kniviel JC, Monache LD, Roux G. Evaluations of WRF sensitivities in surface simulations with an ensemble prediction system. *Atmosphere* 2018;9(3):106.
- [64] Tambke J, Lange M, Focken U, Wolff JO, Bye JAT. Forecasting offshore wind speeds above the North Sea. *Wind Energy* 2005;8:3–16.
- [65] Jimenez B, Durante F, Lange B, Kreutzer T, Tambke J. Offshore wind resource assessment with WAsP and MM5: comparative study for the German Bight. *Wind Energy* 2007;10:121–34.
- [66] Zayas J, Derby M, Gilman P, Ananthan S, Lantz E, Cotrell J, Beck F, Tusing R. *Enabling wind power nationwide*. Washington: DC: U.S. Department of Energy. DOE/EE-1218; 2015. http://energy.gov/sites/prod/files/2015/05/f22/Enabling_Wind_Power_Nationwide_18MAY2015_FINAL.pdf. [Accessed 28 October 2019].
- [67] North CNN. South Korean leaders hold historic summit: Highlights. 2018. <https://edition.cnn.com/asia/live-news/north-korea-south-korea-summit-intl/index.html>. [Accessed 5 June 2018].
- [68] Ghimire S, Deo RC, Downs NJ, Raj N. Self-adaptive differential evolutionary extreme learning machines for long-term solar radiation prediction with remotely sensed MODIS satellite and Reanalysis atmospheric products in solar-rich cities. *Remote Sens Environ* 2018;212:176–98.
- [69] Ghimire S, Deo RC, Raj N, Mi J. Deep solar radiation forecasting with convolutional neural network and long short-term memory network algorithms. *Appl Energy* 2019;253:113541.
- [70] Salcedo-Sanz S, Deo RC, Cornejo-Bueno L, Camacho-Gómez C, Ghimire S. An efficient neuro-evolutionary hybrid modelling mechanism for the estimation of daily global solar radiation in the Sunshine State of Australia. *Appl Energy* 2018;209:79–94.
- [71] Ghimire S, Deo RC, Raj N, Mi J. Wavelet-based 3-phase hybrid SVR model trained with satellite-derived predictors, particle swarm optimization and maximum overlap discrete wavelet transform for solar radiation prediction. *Renew Sustain Energy Rev* 2019;113:109247.
- [72] Deo RC, Sahin M. Forecasting long-term global solar radiation with an ANN algorithm coupled with satellite-derived (MODIS) land surface temperature (LST) for regional locations in Queensland. *Renew Sustain Energy Rev* 2017;72:828–48.